ROYAL SOCIETY
OF CHEMISTRY

EDGE ARTICLE

Check for updates

All publication charges for this article have been paid for by the Royal Society of Chemistry

Revealing hydrogen spillover pathways in reducible metal oxides†

Kazuki Shun,[a] Kohsuke Mori, [ID] *[abc] Shinya Masuda,[a] Naoki Hashimoto,[a] Yoyo Hinuma, [ID] [d] Hisayoshi Kobayashi [ID] [e] and Hiromi Yamashita [ID] *[abc]

Hydrogen spillover, the migration of dissociated hydrogen atoms from noble metals to their support materials, is a ubiquitous phenomenon and is widely utilized in heterogeneous catalysis and hydrogen storage materials. However, in-depth understanding of the migration of spilled hydrogen over different types of supports is still lacking. Herein, hydrogen spillover in typical reducible metal oxides, such as TiO_2, CeO_2, and WO_3, was elucidated by combining systematic characterization methods involving various *in situ* techniques, kinetic analysis, and density functional theory calculations. TiO_2 and CeO_2 were proven to be promising platforms for the synthesis of non-equilibrium RuNi binary solid solution alloy nanoparticles displaying a synergistic promotional effect in the hydrolysis of ammonia borane. Such behaviour was driven by the simultaneous reduction of both metal cations under a H_2 atmosphere over TiO_2 and CeO_2, in which hydrogen spillover favorably occurred over their surfaces rather than within their bulk phases. Conversely, hydrogen atoms were found to preferentially migrate within the bulk prior to the surface over WO_3. Thus, the reductions of both metal cations occurred individually on WO_3, which resulted in the formation of segregated NPs with no activity enhancement.

Introduction

Hydrogen spillover is an interfacial dynamic behaviour, which is initiated by the dissociation of gaseous hydrogen molecules at noble metal sites (*e.g.*, Pt, Pd, and Ru). Spontaneously, the activated hydrogen atoms migrate to the adjacent hydrogen-poor surface driven by a concentration gradient.[1–5] At the metal–support interface, the protons (H^+) diffuse to O^{2-} anions to form O–H bonds, whereas the concurrently generated electrons (e^-) reduce metal cations adjacent to O–H bonds.[1,6] Principally, this process is governed by the following reaction: $M^{n+} + O^{2-} + H \rightarrow M^{(n-1)+} + OH^-$. Because of the facile reduction of metal cations, hydrogen spillover is specific for reducible metal oxides, such as TiO_2,[7–10] CeO_2 (ref. 11–13) and WO_3,[14–16] while it is energetically difficult over non-reducible metal oxides.[17]

[a] Division of Materials and Manufacturing Science, Graduate School of Engineering, Osaka University, 2-1 Yamadaoka, Suita, Osaka 565-0871, Japan. E-mail: mori@mat.eng.osaka-u.ac.jp; yamashita@mat.eng.osaka-u.ac.jp

[b] Unit of Elements Strategy Initiative for Catalysts Batteries (ESICB), Kyoto University, Katsura, Kyoto 615-8520, Japan

[c] Innovative Catalysis Science Division, Institute for Open and Transdisciplinary Research Initiatives (ICS-OTRI), Osaka University, Suita, Osaka 565-0871, Japan

[d] Department of Energy and Environment, National Institute of Advanced Industrial Science and Technology (AIST), 1-8-31, Midorigaoka, Ikeda, Osaka 563-8577, Japan

[e] Kyoto Institute of Technology, Matsugasaki, Sakyo-ku, Kyoto, 606-8585, Japan

† Electronic supplementary information (ESI) available. See https://doi.org/10.1039/d2sc00871h

The detailed mechanism and the utilization of the hydrogen spillover effect have been continually studied since the first report by Khoobiar in 1964.[18] It is undergoing a revival of interest, because unprecedented functions that seem to involve hydrogen spillover have been observed not only in the field of catalysts,[19–24] but also in the fields of hydrogen fuel cells,[25] hydrogen storage materials,[26–28] and hydrogen sensors.[29,30] In order to extend the opportunities for utilizing the spillover effect and developing advanced hydrogen energy devices, comprehensive understanding is indispensable.

Recently, several studies have been performed to further deepen the knowledge of the unique behaviour of hydrogen spillover. Bokhoven and coworkers quantified the spatial extent of hydrogen migration on Al_2O_3 and TiO_2 by observing the reduction of supported iron oxides located at precisely varied distances from co-supported Pt by X-ray absorption fine structure (XAFS) analysis.[6] The results demonstrated that hydrogen spillover over reducible metal oxide TiO_2 is ten orders of magnitude faster than over non-reducible metal oxide Al_2O_3, and enables the reduction of iron oxide located more than 1 μm away from Pt. Zheng *et al.* reported the effect of the support structure on the spillover hydrogenation by utilizing two different exposed facets of Cu (111) and Cu (100) involving dispersed Pd atoms.[31] It was found that hydrogen atoms spilled from Pd atoms only on Cu (100) were active for the semi-hydrogenation of alkynes, although hydrogen spillover from Pd to Cu was facet independent. Furthermore, novel low-temperature catalytic reactions using surface protonics, which

is regarded as hydrogen migration activated by an electric field, have been achieved, in which the migrated H^+ atoms play a crucial role in activating the robust C–H and N≡N triple bonds.[32,33]

In addition to the above experiments, *in situ* characterization techniques, including low-temperature scanning tunneling microscopy (LT-STM),[34] near-ambient pressure X-ray photoelectron spectroscopy (NAP-XPS),[35,36] and tip-enhanced Raman spectroscopy combined with scanning tunneling microscopy (STM-TERS),[37] have been used for real-time monitoring of the hydrogen spillover effect.[37] Despite accumulated reports concerning hydrogen spillover, its dynamic behaviour, such as at what temperature it can take place, what pathway it follows, and the region to where hydrogen migrates, is still poorly understood even for typical reducible metal oxides, because the detailed spillover mechanism is influenced by the difference in reducibility of the metal cations, number of oxygen vacancies and/or surface hydroxyl groups, and the crystal structure.[5,38]

Our group has succeeded in the synthesis of binary solid solution alloy NPs catalysts with essentially immiscible metal combinations (Ru–Ni and Rh–Cu) by utilizing spilled hydrogen atoms as a strong reductant.[39–41] On the other hand, non-reducible γ-Al_2O_3 and MgO supports, whose hydrogen spillover abilities are inferior to that of TiO_2, afforded segregated NPs under the identical synthetic conditions. This means that the formation of non-equilibrium solid solution alloys strongly reflects the hydrogen spillover ability of the support surface. In this study, we first used the above phenomena to identify hydrogen spillover in typical reducible metal oxides, such as TiO_2, CeO_2, and WO_3. The obtained results were further discussed based on systematic *in situ* characterization techniques, kinetic analysis, and density functional theory (DFT) calculations. The combined experiments revealed that TiO_2 and CeO_2 allowed the preferential migration of dissociated hydrogen atoms over their surfaces, whereas hydrogen atoms preferably migrated within the bulk over WO_3. This study provides not only fundamental insights into the spillover pathways but also new strategies for utilizing hydrogen spillover for the design of advanced materials for the up-coming hydrogen society.

Results & discussion

Formation of RuNi solid solution alloy nanoparticles assisted by hydrogen spillover

Ru exists as a hexagonal close-packed (hcp) structure, while Ni exists as a face-centered cubic (fcc) structure in a bulk state, which makes it difficult to form the RuNi solid solution alloy NPs due to their positive enthalpy of mixing. Actually, Ru and Ni are thermodynamically stable in segregation even at 773 K under most of equilibrium composition. Recently, Chen *et al.* succeeded in the synthesis of RuNi solid solution alloy NPs by a hot-injection method with co-reduction of $Ni(acac)_2$ and $Ru(acac)_3$ (acac = acetylacetonate) in oleylamine with super hydride ($LiBEt_3H$) as the reducing agent at 300 °C.[42] Note that if a weaker reducing agent (such as $NaBH_4$) is used, separate growth of Ni and Ru NPs was confirmed. Thus a strong reducing agent, high temperature, and a high-boiling solvent were indispensable for achieving the formation of RuNi solid solution alloy NPs.

We have previously demonstrated that spilled H atoms enabled the simultaneous reduction of deposited Ru^{3+} and Ni^{2+} ions with distinctly different redox potentials to form non-equilibrium RuNi solid solution alloy NPs. TiO_2, one of the typical reducible metal oxides, was shown to be a promising platform for the formation of RuNi NPs due to its prominent hydrogen spillover ability associated with the concurrent proton–electron transfer.[39,40] On the other hand, non-reducible metal oxides, such as Al_2O_3, and MgO, were demonstrated not to be suitable owing to the lack of hydrogen spillover on their surfaces. The formation of RuNi solid solution alloy NPs was confirmed by HR-TEM and EDX analysis, in which Ru and Ni were randomly distributed over RuNi/TiO_2 without segregation (Fig. S1†). Moreover, RuNi/TiO_2 showed drastically improved activity during the hydrolysis of ammonia borane (AB) compared to monometallic Ru/TiO_2, even though Ni exhibited only negligible activity at the same condition. This synergistic promotional effect is attributed to neighboring Ru–Ni pairs with an electronic imbalance, as proven by DFT calculations (Fig. S2†).[40]

Thus, the catalytic performance of each catalyst during the hydrolysis of AB is strongly reflected by whether the RuNi solid solution alloy NPs are formed or not, which may be conventionally utilized as a method for evaluating the surface hydrogen spillover ability of a series of reducible metal oxides, such as TiO_2, Ga_2O_3, CeO_2, Nb_2O_5, and WO_3. Ru and Ni were deposited on each support by an impregnation method and subsequently reduced under H_2 atmosphere at 300 °C. The mean particle diameters of RuNi catalysts over TiO_2 and WO_3 were comparable with those obtained for the monometallic Ru catalysts (Fig. S2 and S3†). The particles sizes of RuNi and Ru over the CeO_2 catalysts cannot be defined because of its heavy characteristic, but the elemental mapping indicates the high dispersion of Ru and Ni species without agglomeration (Fig. S4†). These results clearly exclude the effect of particle size on catalytic activity.

The time courses of hydrogen evolution during the hydrolysis of AB ($NH_3BH_3 + 2H_2O \rightarrow NH_4^+ + BO_2^- + 3H_2$) are shown in Fig. 1a–e. Fig. 1f summarizes the normalized turnover frequency (TOF) values for RuNi catalysts based on Ru. Notably, the reactions using pure Ni catalysts were extremely sluggish, regardless of the supports. The activity enhancement ratio was strongly dependent on the reducibility of the catalyst supports, which was determined by Helali and coworkers based on the formation energy of oxygen vacancies.[43]

RuNi supported on TiO_2, Ga_2O_3, and CeO_2 catalysts, with relatively low reducibility, showed enhanced activity over those of the corresponding monometallic Ru catalysts by a factor of approximately 2, suggesting the formation of RuNi solid solution alloy NPs by the assistance of hydrogen spillover on their surfaces. Similarly, the activity of RuNi/Nb_2O_5 was 1.5 times higher than that of Ru/Nb_2O_5. By contrast, RuNi/WO_3 did not show any improvement in the activity by the addition of Ni, which indicates that no RuNi solid solution alloy was formed on the surface of WO_3 despite its high reducibility, as will be
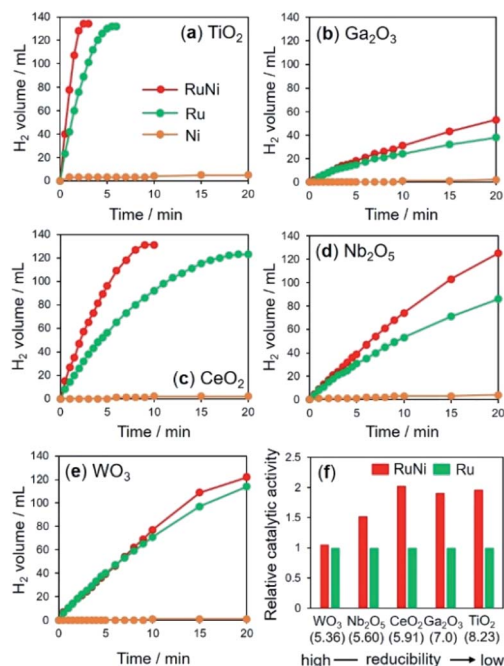
Fig. 1 Time course of hydrogen evolution in hydrolysis of AB over metal-supported (a) TiO_2, (b) Ga_2O_3, (c) CeO_2, (d) Nb_2O_5, and (e) WO_3, and (f) activity enhancement for each catalyst by the addition of Ni. The values in parentheses in (f) are the formation energies of oxygen vacancies (eV) determined by DFT calculations.

discussed later. For subsequent detailed characterizations, we used TiO_2, CeO_2, and WO_3 as typical supports in an effort to investigate the hydrogen spillover ability.

H$_2$-TPR measurements were performed to evaluate the reduction behaviour of each sample (Fig. 2a). The reduction

Fig. 2 (a) H$_2$-TPR profiles of Ru, Ni or RuNi-supported (i) TiO_2, (ii) CeO_2, (ii) WO_3. (b) Ru K-edge XANES spectra and (c) Ru K-edge FT-EXAFS spectra of (i) RuNi/TiO_2, (ii) RuNi/CeO_2, (iii) RuNi/WO_3, and (iv) Ru foil.

peaks for Ni^{2+} ions of as-deposited Ni samples appeared at much higher temperature than those for Ru^{3+} in Ru deposited samples for all supports (Table 1). These results are reasonable because Ru^{3+} ions are easier to reduce than Ni^{2+} ions due to their higher reduction potential $(E_0(Ni^{2+}/Ni) = -0.26$ V vs. NHE, $E_0(Ru^{3+}/Ru) = 0.80$ V vs. NHE). Interestingly, both Ru^{3+}- and Ni^{2+}-deposited TiO_2 and CeO_2 showed only one peak with a maximum at around 158 °C and 126 °C, respectively. These results suggest that hydrogen spillover occurs at low temperature on TiO_2 and CeO_2, which promotes the reduction of Ni^{2+} ions, and then both Ru^{3+} and Ni^{2+}ions were simultaneously reduced to form a RuNi solid-solution alloy despite the difference in redox potentials. On the other hand, RuNi/WO_3 showed several peaks attributed to the reduction of Ru^{3+} and Ni^{2+} species. Such reduction profiles indicate that hydrogen spillover on WO_3 occurs at much higher temperature than the reduction temperature of only Ru^{3+}, which cause sequential reduction of Ru^{3+} and Ni^{2+} ions, resulting in segregated NPs rather than solid solution alloy ones.

In the separate experiments, Ni^{2+}-deposited samples including pre-reduced Ru NPs was employed. The details were summarized in Fig. S5.† The CO pulsed measurement and TEM analysis indicated that no significant differences were found in the dispersion and particle sizes of Ru NPs on each support. The reduction temperature of the Ni^{2+} ions on TiO_2 and CeO_2 were substantially decreased in the presence of pre-reduced Ru NPs. On the other hand, the reduction temperature of Ni^{2+} ions on WO_3 was not promoted even in the presence of pre-reduced Ru NPs. These results exclude the effect of particle size on the reduction of metals due to the hydrogen spillover.

In order to distinctly assess the reduction sequences, in situ XAFS measurements were performed under H_2 atmosphere at elevated temperature. The reduction temperatures for the deposited Ru^{3+} and Ni^{2+} were determined from the change in the X-ray absorption near edge structure (XANES) spectra during a reduction sequence (Table 1 and Fig. S6–S8†). In preliminary results, as deposited Ni and Ru species were found to be single-atom in 2+ and 3+ oxidation states for all samples, respectively (Fig. S9†). Additionally, the reduction temperatures of Ni^{2+} and Ru^{3+} ions for monometallic samples were not dependent on the
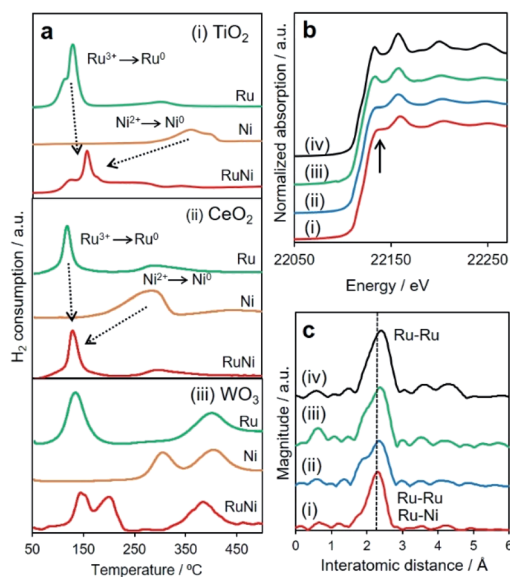
Table 1 Reduction temperatures for Ru^{3+} and Ni^{2+} supported on TiO_2, CeO_2 and WO_3 as determined based on in situ XANES spectra and H_2-TPR

Sample	H$_2$-TPR	In situ XANES spectra	
		Ru K-edge	Ni K-edge
Ru/TiO_2	130 °C	125 °C	—
Ni/TiO_2	370 °C	—	325 °C
RuNi/TiO_2	160 °C	200 °C	200 °C
Ru/CeO_2	125 °C	150 °C	—
Ni/CeO_2	300 °C	—	330 °C
RuNi/CeO_2	125 °C	190 °C	200 °C
Ru/WO_3	130, 405 °C	140 °C	—
Ni/WO_3	310, 405 °C	—	320 °C
RuNi/WO_3	145, 200, 390 °C	170 °C	240 °C

support materials. These results indicate that the effect of interaction between metal precursors and supports on spillover effect can be excluded. It should be noted that the reduction temperatures for Ru^{3+} slightly increased in the presence of Ni^{2+}, while the reduction temperature of Ni^{2+} drastically decreased in the presence of Ru^{3+} for all samples. More importantly, the reduction temperatures for Ni^{2+} and Ru^{3+} ions were nearly consistent for $RuNi/TiO_2$ and $RuNi/CeO_2$. In contrast, the reduction temperatures for Ru^{3+} and Ni^{2+} species on the surface of WO_3 were determined to be 170 °C and 240 °C, respectively, suggesting the subsequent reduction of Ru^{3+} followed by Ni^{2+}. These results are all consistent with the H_2-TPR results and clearly indicate that TiO_2 and CeO_2 allow a more rapid and homogeneous reduction at lower temperatures driven by the pronounced hydrogen spillover effect in comparison to WO_3. The retarded reducibility of the Ru^{3+} species in the presence of Ni^{2+} in comparison with that for the monometallic samples over the TiO_2 and CeO_2 supports may be ascribed to the interaction between Ru^{3+} and Ni^{2+} and the decrease of the coverage of the Ru^{3+}.

A comparison of the X-ray absorption results after reduction at 300 °C provides additional local structural information. The shapes of the normalized XANES spectra at the Ru K-edge and the edge positions for three RuNi samples resembled those of Ru foil (Fig. 2b). More detailed inspection revealed that the intensity of two distinct peaks at approximately 22 136 and 22 159 eV for $RuNi/TiO_2$ and $RuNi/CeO_2$ were different from those for $RuNi/WO_3$ and Ru foil, indicating that the symmetry of the Ru metal hcp structure was slightly disordered by integration with the Ni.[44] The Ru K-edge Fourier transform-extended X-ray absorption fine structure (FT-EXAFS) spectra contained a single sharp peak associated with Ru–Ru bonds at approximately 2.4 Å (Fig. 2c). For $RuNi/TiO_2$ and $RuNi/CeO_2$, the position of this peak was slightly shifted to shorter interatomic distances in comparison with Ru foil, which suggests the formation of heteroatomic Ru–Ni bonding. Moreover, the inverse FT was well fitted by using Ru–Ru and Ru–Ni shells, respectively (Table 2 and Fig. S10†). On the other hand, no shift of the main peak was observed for $RuNi/WO_3$, in which curve fitting was completed with only Ru–Ru bonds without the contribution of Ru–Ni bonds. EDX analysis of $RuNi/WO_3$ showed the random distribution of Ru and Ni, and the formation of definite RuNi solid solution alloy was not observed (Fig. S12†). Conclusively, the RuNi alloy NPs were evidently formed not only on TiO_2, but also on CeO_2, while Ru^{3+} and Ni^{2+} species were reduced separately on the surface of WO_3, which

results in the formation of segregated NPs rather than the solid solution alloy.

Mechanistic investigation by DFT calculations

Considering the H_2-TPR and *in situ* XAFS results, a mechanism for the formation of the RuNi solid solution alloy NPs in conjunction with hydrogen spillover is proposed in Fig. 3a. The Ru^{3+} precursors are first partially reduced to generate nuclei, which then act as uptake sites to dissociate H_2 to form Ru–H species (step 1). The reduction of M^{n+} to $M^{(n-1)+}$, together with the transfer of H atoms from Ru nuclei at the metal–support interfaces (step 2), is accompanied by the migration of electrons from $M^{(n-1)+}$ ions to neighboring M^{n+} ions. This promotes the subsequent simultaneous transfer of protons to O^{2-} anions attached to these adjacent M^{n+} ions (step 3). In this manner, hydrogen atoms rapidly reduce all metal ions by moving over the support surface (step 4).

DFT calculations were performed to simulate the activation energies for each step. Rutile TiO_2 (110), CeO_2 (001), and WO_3 (001) were employed as the models of supports due to their superior stability. Ru_5 clusters with a square pyramidal arrangement were chosen as Ru nuclei because 5 is the magic number for Ru_n clusters.[45,46] The energy diagram and the obtained activation energy (E_a) are displayed in Fig. 3b and Table 3, in which step 1 (I → II), step 2 (II → III), step 3 (III′ → IV), and step 4 (IV′ → V) were considered as the representative
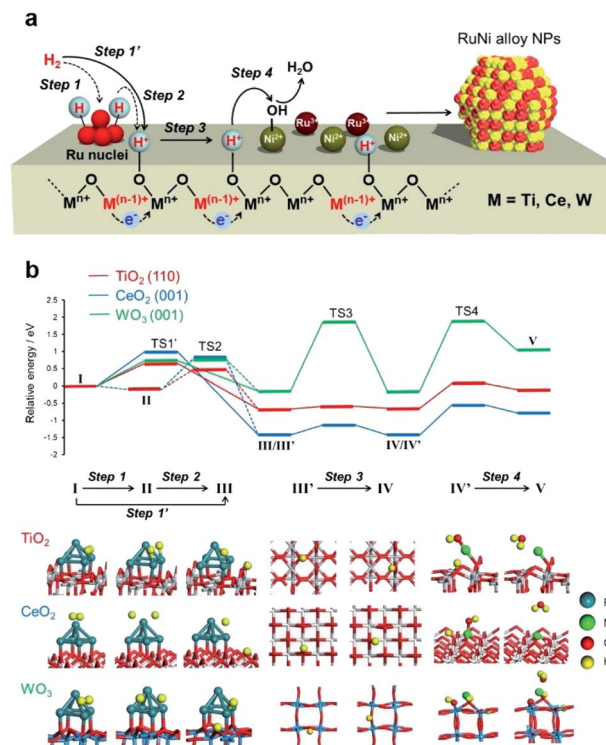

Fig. 3 (a) Schematic illustration of elementary steps in formation of solid solution alloy NPs on reducible metal oxides support assisted by hydrogen spillover and (b) potential energy profiles for processes on TiO_2 (110), CeO_2 (001), and WO_3 (001) as obtained from DFT calculations.

Table 2 Curve fitting results determined by Ru K-edge FT-EXAFS data

	Shell	CN	R/Å	σ^2
$RuNi/TiO_2$	Ru–Ru	5.4	2.64	0.0064
	Ru–Ni	4.2	2.54	0.0056
$RuNi/CeO_2$	Ru–Ru	3.7	2.63	0.0077
	Ru–Ni	2.0	2.59	0.0022
$RuNi/WO_3$	Ru–Ru	6.4	2.65	0.0056

Table 3 Activation energies (E_a; eV) for various steps during hydrogen spillover on TiO_2, CeO_2, and WO_3

	Step 1 (I → II)	Step 2 (II → III)	Step 3 (III → IV)	Step 4 (IV → V)	Step 1' (I → III)	Step 4'
	H_2 cleavage on Ru_5 (homolytic)	H atom transfer from Ru_5 to oxide	H atom migration on oxide	Reduction of Ni^{n+} by spilled H (Langmuir–Hinshelwood mechanism)	H_2 cleavage on Ru_5 and oxide (heterolytic)	Reduction of Ni^{n+} by H_2 vapor (Eley–Rideal mechanisms)
TiO_2 (110)	$\sim 0.0^a$	0.92	0.08	0.72	0.66	3.69
CeO_2 (001)	$\sim 0.0^a$	1.31	0.28	0.87	1.00	2.54
WO_3 (001)	$\sim 0.0^a$	1.26	2.04	2.01	0.73	5.16

^{a} The H_2 molecule was dissociated spontaneously upon adsorption on a Ru atom away from the Ru5/support interfaces.

elementary steps in the hydrogen spillover process. Energy profiles and calculated models were shown in Fig. S11–S23.†

The activation energies (E_a) in the dissociation of H_2 at Ru_5 (step 1) are barrier-less for all models. The H_2 molecule was dissociated spontaneously upon adsorption on a Ru atom away from the Ru_5/support interfaces.[47] In the case of TiO_2 (110), the E_a of step 2 was calculated to be 0.92 eV. Alternatively, the heterolytic H_2 splitting at the metal–support interface (denoted as step 1' (I → III) in Table 3) was calculated to be 0.66 eV, indicating that this is the energetically more reasonable pathway than the homolytic H_2 splitting at the Ru followed by the migration from Ru to supports.[47] The migration of a H atom (step 3) over the TiO_2 (110) is energetically favourable between 3-coordinated oxygen atom and 2-coordinated one (Fig. S13†). The E_a of 0.72 eV for step 4 was the largest among the four steps, suggesting that reduction of Ni^{n+} by the spilled H atom is rate-determining. A relatively low E_a for all steps indicates the easy occurrence of hydrogen spillover over TiO_2 without a large external energy input. In the case of CeO_2, step 1 was barrier-less and the E_a values for step 3 was small, whereas that of step 2 was 1.31 eV. The heterolytic H_2 splitting pathway (step 1') was determined to be 1.00 eV, indicating the involvement of the energetically reasonable alternative pathway. The H atom migration on this substrate (step 3) preferentially occurs at the nearest oxygen sites, and there is a relatively high activation energy for migration to the secondary-adjacent oxygen site (Fig. S17†). In contrast, step 3 was found to be the rate-determining step for WO_3 and the E_a was as large as 2.04 eV for possible two pathways (Fig. S19†).

Adsorption of neutral H on the surface could, in some cases, be more appropriately described as adsorption of H^+ and e^-, and the excess electron may be localized on a metal nanoparticle at the surface.[48] A related phenomenon where excess electrons appear at the surface is surface O removal as a neutral species. The surface O vacancy formation energy can be reduced when a nearby metal nanoparticle can absorb excess electrons (electron scavenger effect).[49] Hinuma et al. showed that manifestation of the electron scavenger effect is determined by the order of the oxide defect level after O removal and the metal work function.[50] Compared to late transition metals typically

adsorbed as nanoparticles, fully oxidized group 3, 4, 5 oxides as well as CeO_2 have very large ionization potentials (IPs), or in other words, the valence band maximum is very deep with respect to the vacuum level. However, the IPs become smaller when the cation is reduced. In particular, reduced titanium oxides have very small IPs and the electron scavenger effect could happen, which could explain the surface reactivity of reduced oxides. That being said, diffusion of H over long distances of the TiO_2 surface requires diffusion over regions where nanoparticles are far away and are less reduced. We focused on calculating the activation barrier in such regions because this would become the bottleneck.

The reduction of deposited Ni^{n+} ions by the spilled H atoms (step 4) was qualitatively evaluated by calculating E_a for the attack of a neighbouring H atom on a Ni^{n+}–OH species on the support, together with the loss of H_2O. The Mulliken atomic charges of Ni atom decreased after the reduction for all models (Fig. S23–S25†), suggesting the reduction of Ni atoms. The electron density in the vicinity of the Fermi level ($E = 0$) clearly increased after the reduction of Ni species, suggesting the change of oxidation state of Ni atoms from oxide to metallic nature (Fig. S24†). These E_a values according to Langmuir–Hinshelwood mechanism were estimated to be 0.72, 0.87, and 2.01 eV for TiO_2 (110), CeO_2 (001), and WO_3 (001), respectively, which are substantially lower than those for the same process by the direct reduction with a gaseous H_2 molecule (step 4' in Table 3; 3.69 eV for TiO_2 (110), 2.54 eV for CeO_2 (001), and 5.16 eV for WO_3 (001), which follows Eley–Rideal mechanisms, as shown in Fig. S25†). Consequently, the order of E_a in the rate-determining steps is TiO_2 (110) < CeO_2 (001) < WO_3 (001) and the TiO_2 and CeO_2 surfaces do not require a higher energy input than that on WO_3 for the formation of RuNi alloy NPs by the assist of hydrogen spillover, despite the stronger binding energy of metals over TiO_2 and CeO_2 rather than WO_3 (Table S1 and Fig. S26†). Moreover, the E_a for the removal of lattice oxygen by the spilled H atoms to form H_2O and oxygen vacancy were 3.60 eV for TiO_2 (110), 3.09 eV for CeO_2 (001), and 2.40 eV for WO_3 (001) (Fig. S27†), which were substantially larger than those in step 4. This verified that spilled H atoms promoted the rapid and simultaneous reduction of the metal precursors at

low temperatures, and the reduction of metal cations of support themselves is negligible on a thermodynamic basis.
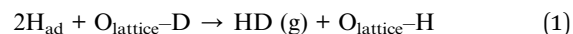
Identification of surface and internal hydrogen spillover

In the hydrogen spillover process, the dissociated hydrogen atoms generate O–H bonds *via* a concurrent proton–electron transfer pathway. We evaluated the hydrogen spillover characteristics on the surface of Ru-supported TiO_2, CeO_2 and WO_3 by *in situ* DRIFT experiments after D_2 introduction at 50, 150, and 250 °C. Ru/TiO_2 generated a distinct peak assignable to δ_{O-D} stretching vibrations ranging from 2550–2750 cm^{-1} at 50 °C, as displayed in Fig. 4.[51,52] No peaks were detected for Ru/CeO_2 or Ru/WO_3 at 50 °C, suggesting the absence of hydrogen spillover, while peaks appeared at 150 °C for Ru/CeO_2 and 250 °C for Ru/WO_3. It should be noted that this characteristic peak cannot be observed in the intrinsic metal oxides without Ru, indicating that formation of δ_{O-D} definitely originated from hydrogen spillover *via* the supporting Ru, not the direct insertion of gaseous H_2. These results prove that hydrogen spillover occurred at different temperatures depending on the metal oxides, *i.e.*, TiO_2 (below 50 °C), CeO_2 (50–150 °C), and WO_3 (150–250 °C), which supports the above experimental results for the formation of RuNi solid solution alloy NPs and theoretical calculations. Moreover, the BET surface areas (S_{BET}) determined by N_2 adsorption–desorption were TiO_2 (60.1 m^2 g^{-1}), CeO_2 (135.3 m^2 g^{-1}), and WO_3 (5.5 m^2 g^{-1}), respectively. This means that the hydrogen spillover on WO_3 is slow albeit the coverage of Ru is quite high, which further verify that the hydrogen spillover on TiO_2 and CeO_2 favourably occur than that on WO_3.

The reducibility (formation energy for oxygen vacancies) of WO_3 (5.36 eV) is higher than those of TiO_2 (8.23 eV) and CeO_2 (5.91 eV). However, the results described above demonstrated that H atom transfer on WO_3 is energetically more difficult than

Fig. 4 *In situ* DRIFT experiments following D_2 for (a) Ru/TiO_2, (b) CeO_2, and (c) WO_3. The specimen was first heated under N_2 at 150 °C for 1 h to remove physisorbed water. Subsequently, H_2 gas was introduced into the specimen at 50 °C and a baseline was collected, and then the gas was switched to D_2 and kept for 10 min to equilibrate. The H_2–D_2 switching process was performed and spectra were obtained at 50 °C, 150 °C, and 250 °C.

that on TiO_2 and CeO_2. In order to understand this contradiction, we must consider the hydrogen spillover pathway not only from the surface but also from the bulk point of view, because the obtained results for the formation of RuNi alloy NPs and DFT calculations are essentially reflected by the hydrogen spillover pathway on the surface of metal oxides.

By employing Ru/TiO_2, Ru/CeO_2 and Ru/WO_3 as specimens, H/D exchange *via* the spillover process was monitored at elevated temperature, and the reaction can be simply described as

$$2H_{ad} + O_{lattice}\text{–}D \rightarrow HD\ (g) + O_{lattice}\text{–}H \tag{1}$$

where H_{ad} is adsorbed H atom, $O_{lattice}$ is lattice oxygen in metal oxides and HD (g) is the yielded gaseous HD. Specifically, the specimen was first heated at 300 °C under a D_2 atmosphere to introduce O–D bonds into/onto each support. Subsequently, the specimen was cooled to room temperature and heated to 400 °C at a rate of 5 °C min^{-1} under a H_2 atmosphere, and the formed HD ($m/z = 3$) was detected by mass spectrometry (MS).

All samples showed an immediate HD production peak at low temperature after switching to H_2, which originated from H/D exchange at the Ru NPs, not on the metal oxides related to hydrogen spillover. Ru/TiO_2 showed strong peaks at around 50 °C accompanied by a small peak at around 100 °C (Fig. 5a). Our DRIFT experiment revealed that Ru/TiO_2 produced O–D bonds *via* hydrogen spillover at lower than 50 °C. Moreover, it has been reported that hydrogen atoms can quickly migrate more than 1 μm over a TiO_2 surface.[6] Thus, the peak observed at lower temperature can be assigned to the HD formed on the surface, while the peak at higher temperature is assignable to the HD formed in the bulk (internal phase). Notably, the contribution from the bulk is small, indicating that migration of hydrogen atoms is limited to the subsurface of TiO_2 (the second O–Ti–O tri-layer) at less than 300 °C. Similarly, Ru/CeO_2 displayed a bimodal peak involving a prominent peak at 90 °C and a minor peak at 230 °C (Fig. 5b). The slight shift of both peaks toward higher temperatures indicates slower H/D exchange compared to TiO_2, which is in agreement with the DRIFT experiment.

Interestingly, Ru/WO_3 showed only one peak at 130 °C (Fig. 5c). This temperature was substantially lower than that observed by *in situ* DRIFT, where the δ_{O-D} bond appeared at 250 °C. From the XRD pattern after H_2 reduction at 150 °C, the crystal structure of Ru/WO_3 was completely changed from monoclinic WO_3 (JCPDS No. 43-1035) to $W_{19}O_{55}$ (JCPDS No. 45-0167) by the introduction of oxygen vacancies (Fig. S28†).[53] Moreover, a significant colour change from white to bronze, which is due to the appearance of mixed valence transfer bands between W^{6+} and W^{5+},[14,15] can be observed in the *in situ* UV-vis measurements under H_2 flow at temperatures between 70 °C and 180 °C (Fig. S29†). This temperature range matches well with that of the HD production peaks *via* H–D exchange (Fig. 5c). These supplementary results clearly confirmed that the peak observed at around 130 °C can be assigned to the HD formed *via* internal hydrogen spillover within the bulk, and hydrogen spillover over WO_3 preferentially occurs within the
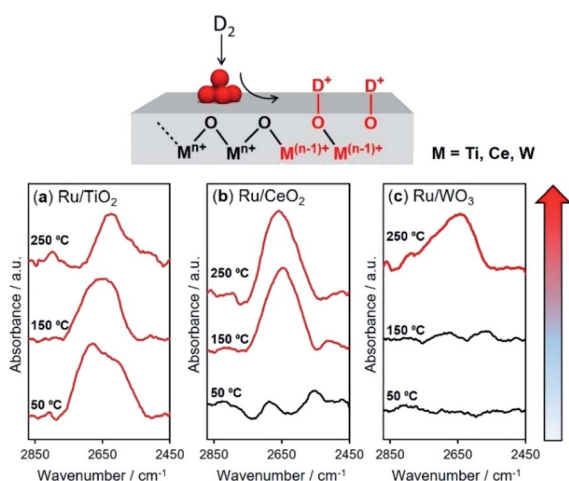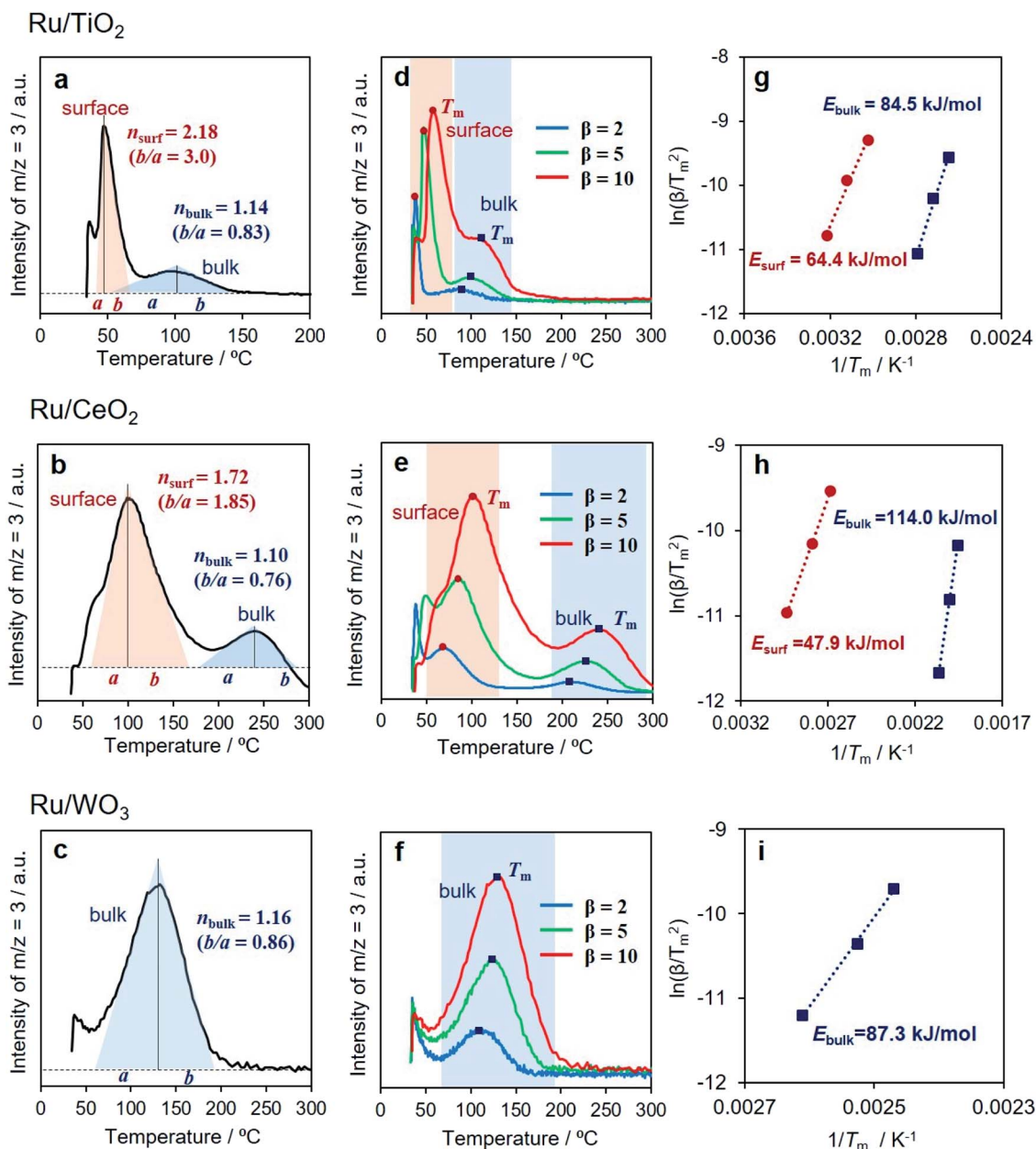
Fig. 5 HD evolution as function of heating rate β (°C min^{-1}) monitored by mass spectrometry for (a) Ru/TiO$_2$, (b) Ru/CeO$_2$, and (c) Ru/WO$_3$, determination of reaction order from asymmetry of endothermic differential thermal analysis peak for (d) Ru/TiO$_2$, (e) Ru/CeO$_2$, and (f) Ru/WO$_3$, and Kissinger plots to evaluate activation energies of H/D exchange processes for (g) Ru/TiO$_2$, (h) Ru/CeO$_2$, and (i) Ru/WO$_3$.

bulk phase accompanied by partial reduction of W^{6+} to W^{5+} rather than on the surface.

It should be noted that there is an obvious difference in the shape of both peaks for Ru/TiO$_2$ and Ru/CeO$_2$ (Fig. 5d and e). Kissinger reported that the symmetry of the peaks obtained by differential thermal analysis gave the reaction order (n) according to the following equation:[54]

$$n = 1.26\sqrt{S} \quad \left(S = b/a\right) \qquad (2)$$

where S is the shape index defined by the peak symmetry (Fig. S30†). As a result, the reaction orders on the surface (n_{surf})

were calculated to be 2.18 and 1.72, while those within the bulk (n_{bulk}) were determined to be 1.14 and 1.10 for Ru/TiO$_2$ and Ru/CeO$_2$, respectively (Fig. 5a and b). This means that the reaction orders for the H/D exchange reaction are essentially dependent on the spillover site (surface or bulk), not on the type of reducible metal oxides. The reaction order obtained from the peak of Ru/WO$_3$ was 1.16 (Fig. 5c), which is consistent with those within the bulk observed in Ru/TiO$_2$ and Ru/CeO$_2$. This further verifies that H/D exchange *via* the spillover process of WO$_3$ is dominated within the bulk. The differences in the reaction order are presumably due to the differences in the

coordination number of oxygen atoms and geometry over the surface and within the bulk.

Furthermore, the H/D exchange *via* spillover process was analyzed by applying the Kissinger equation given by

$$\ln\frac{\beta}{T_m^2} = -\frac{E_a}{R}\frac{1}{T_m} + \ln A \qquad (3)$$

where β is the heating rate, T_m is the peak temperature, E_a is the activation energy, and R is the universal gas constant. Kobayashi and Kageyama *et al.* experimentally determined E_a for hydride diffusion involving H/D exchange in perovskite oxyhydrides according to the Kissinger method.[55] For all samples, T_m shifted to higher temperature along with increasing heating rate and a linear relationship between $\ln(\beta/T_m^2)$ and $1/T_m$ was obtained (Fig. 5g–i). In the case of Ru/TiO$_2$, E_a on the surface ($E_{a,surf} = 64.4$ kJ mol^{-1}) was smaller than that within the bulk ($E_{a,bulk} = 84.5$ kJ mol^{-1}). Ru/CeO$_2$ displayed a similar trend ($E_{a,surf} = 47.9$ kJ mol^{-1} and $E_{a,bulk} = 114.0$ kJ mol^{-1}). These kinetic investigations further demonstrated that hydrogen spillover preferentially occurs on the surface of TiO$_2$ and CeO$_2$ rather than in the bulk after transferring from Ru nuclei at the metal–support interfaces. The $E_{a,surf}$ for Ru/TiO$_2$ was found to be larger than that with Ru/CeO$_2$. This is reasonably supported by the theoretical calculation of the activation energy in step 3 (migration of H atoms). The $E_{a,bulk}$ for Ru/WO$_3$ (87.3 kJ mol^{-1}) is comparable to that obtained with Ru/TiO$_2$, suggesting that the migration of hydrogen atoms within bulk WO$_3$ occurs in a similar temperature range as that in the subsurface in TiO$_2$.

Upon consideration of the above results, a possible reaction pathway for hydrogen spillover over each reducible metal oxide is proposed in Fig. 6. Ru/TiO$_2$ allows preferential hydrogen spillover on its surface at less than 50 °C, which extends to its subsurface from 50 °C to 150 °C (Fig. 6a). The spillover within the bulk does not occur even at higher temperature, because almost no peak due to the formation of HD was observed at higher temperature than even 150 °C (Fig. 5a). Ru/CeO$_2$ also favours hydrogen spillover on its surface in the temperature range from 50 °C to 150 °C, which migrates to its subsurface at higher than 150 °C (Fig. 6b). It can be said that the spillover within the bulk is suppressed at around 250 °C, since the activation energy within the bulk is substantially higher ($E_{a,bulk} = 114.0$ kJ mol^{-1}) (Fig. 5h). In the case of Ru/WO$_3$, hydrogen spillover hardly occurs at less than 50 °C. In the temperature range from 50 °C to 150 °C, H atoms predominantly migrate to within the bulk phase rather than the surface. It can be deduced that a further increase in temperature allows migration to the surface, because the reduction temperature of the deposited Ni^{2+} ions, which is accelerated by surface hydrogen spillover, dropped from 320 to 240 °C in the presence of Ru^{3+} (Table 1).

In order to support the experimental results for the hydrogen spillover pathway, H diffusion energy from the surface to the subsurface was calculated for TiO$_2$ (110), CeO$_2$ (001), and WO$_3$ (001). The results were shown in Fig. S32.† The energy of the H atom migration over TiO$_2$ (110) from the top surface to the first and second inside oxide layers were 0.90 and 1.17 eV, respectively, which were larger than that of the surface H atom migration (0.08 eV, see Table 3). A similar tendency was
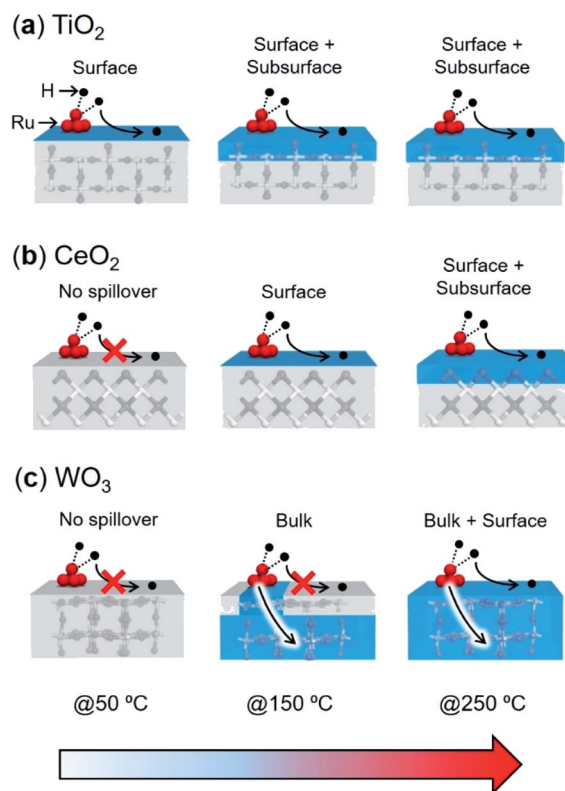

Fig. 6 Proposed spillover pathways for (a) TiO$_2$, (b) CeO$_2$, and (c) WO$_3$ at various temperatures. The blue highlighted shows the H-migrated area.

observed over CeO$_2$ (001). On the contrary, H diffusion from surface to first and second inside oxide layers over WO$_3$ (001) occurs with a barrier of 0.75 and 0.52 eV, respectively, which were substantially lower than that of the surface H atom migration (2.04 eV, see Table 3). These results agree with the experimental data obtained from the DRIFT and HD formation reaction.

With respect to the differences in the hydrogen spillover pathway, we point out the importance of the redox properties of metal oxides, because hydrogen spillover proceeds with concurrent proton–electron transfer associated with reversible reduction and oxidation of metal oxides ($M^{n+} + e^- \leftrightarrow M^{(n-1)+}$). Since TiO$_2$ and CeO$_2$ have moderate reducing properties (the formation energies of oxygen vacancies), the redox of metal oxides is likely to proceed reversibly on their surfaces. Accordingly, hydrogen spillover preferentially occurs on their surfaces, since metal oxides are less likely to be reduced within the bulk due to the increase in the number of coordinated oxygen atoms, resulting in limited hydrogen spillover into the bulk.

The high reducibility of WO$_3$ tends to accelerate the reduction of W^{6+} ions, thus retarding the oxidation of W^{5+} ions. Consequently, hydrogen spillover on the surface of Ru/WO$_3$ is limited because the reversible redox reaction is unlikely to proceed. As the number of adjacent oxygen atoms increases, such a trade-off relationship would be improved. Thus, WO$_3$ allows the reversible reduction and oxidation of W ions within

the bulk and preferentially transfers H atoms. It can be concluded that the reducibility of the metal oxides is responsible for not only the improvement of hydrogen spillover but also its pathway.

Conclusions

We explored the inherent hydrogen spillover properties of three representative reducible metal oxides. Reduction profiles for the deposited ions obtained using H_2-TPR and *in situ* XAFS data suggest the simultaneous reduction of Ru^{3+} and Ni^{2+} species on the TiO_2 and CeO_2 supports, which generates RuNi binary solid solution alloy NPs exhibiting a synergistic effect in AB hydrolysis. These two cations were reduced individually on WO_3, resulting in the formation of segregated NPs without activity enhancement. These results indicated that the hydrogen spillover on the surface of TiO_2 and CeO_2 is more likely proceed than on WO_3. DFT calculations revealed that the rate-determining steps were different, and the activation energy increased in the order of TiO_2 (110) < CeO_2 (001) < WO_3 (001). *In situ* DRIFT and kinetic analysis of HD formation based on the Kissinger method verified that hydrogen spillover on TiO_2 and CeO_2 favorably occurred on their surfaces rather than within their bulk phases. Conversely, hydrogen spillover on WO_3 preferentially proceeded within the bulk prior to the surface. These insights into the occurrence temperature of hydrogen spillover as well as its migration pathway will provide an opportunity to select an optimized metal oxide and maximize its properties according to the desired application fields, such as hydrogen storage, catalysts/photocatalyst design, and enhancement of catalytic functions. Meanwhile, a more in-depth study combined with an experimental approach, theoretical calculation, and advanced characterization should be performed for the construction of key technology in the upcoming hydrogen society.

Experimental

Materials

TiO_2 (JRC-TIO-4, anatase : rutile = 7 : 3), CeO_2 (JRC-CEO-2), and Nb_2O_5 (JRC-NBO-2) were supplied by the Catalysis Society of Japan. WO_3 and Ga_2O_3 were obtained from Wako Pure Chemical Industries, Ltd. $RuCl_3 \cdot nH_2O$ and $NiCl_2 \cdot 6H_2O$ were obtained from Nacalai Tesque. Ammonia borane (AB, NH_3BH_3) was purchased from Aldrich Chemical Co. All commercially available chemicals were used as received. Distilled water was employed as the reaction solvent.

Preparation of catalysts

$RuCl_3 \cdot 3H_2O$ (0.0324 g, 0.124 mmol) and $NiCl_2 \cdot 6H_2O$ (0.038 mmol, Ru : Ni = 1 : 0.3) were added to a mixture of TiO_2 (0.6 g) and distilled water (100 mL). This suspension was stirred at room temperature for 1 h, after which the solvents were evaporated under vacuum. Finally, the sample was reduced under H_2 dosage at a heating rate of 5 °C min^{-1} (20 mL min^{-1}, 300 °C) for 2 h to yield RuNi/TiO_2 (Ru 2.0 wt%; Ru : Ni = 1 : 0.3).

RuNi/CeO_2, RuNi/WO_3, RuNi/Ga_2O_3, and RuNi/Nb_2O_5 with the same Ru and Ni loadings were also prepared by the same procedure.

Characterization

Transmission electron microscopy (TEM) images were obtained with a field emission (FE) TEM instrument (Hf-2000, Hitachi). Scanning transmission electron microscopy (STEM) images, elemental mapping and line analysis were obtained using a JEOL-ARM 200F instrument equipped with a Kevex EDX detector (JED 2300T) operated at 200 kV. Powder X-ray diffraction (XRD) patterns were recorded using a Rigaku Ultima IV diffractometer with Cu Kα radiation (λ = 1.54056 Å). Temperature-programmed reduction with H_2 (H_2-TPR) was conducted on a BEL-CAT (BEL Japan, Inc.) instrument by heating 50 mg specimens at 5 °C min^{-1} from 50 to 600 °C under a 5.0% H_2/Ar flow. Ru K-edge and Ni K-edge *in situ* X-ray absorption fine structure (XAFS) spectra were acquired in transmission mode at the 01B1 beamline station in conjunction with a Si (111) monochromator at SPring-8, JASRI, Harima, Japan (Proposal No. 2020A1062 and 2020A0523). In a typical experiment, spectra were acquired while a pellet sample was held in a batch-type *in situ* XAFS cell. XAFS data were examined using the REX2000 and ATHENA programs (Demeter).[56] *In situ* diffuse reflectance infrared Fourier transform spectroscopy (DRIFTS) measurements were conducted using an IR Spirit (Shimadzu) instrument equipped with a heating chamber connected to a gas-exchange system. HD (*m/z* 3) production *via* the hydrogen spillover process at heating rates of 2, 5 and 10 °C min^{-1} was measured by mass spectrometry (MS) using a BELMass (BEL Japan, Inc.) connected to a BEL-CAT instrument. *In situ* ultraviolet-visible adsorption spectroscopy (UV-vis) measurements were conducted using a V-750 (JACSO International Co., Ltd).

Hydrolysis of AB

In a typical experiment, the RuNi/TiO_2 catalyst (10 mg) and distilled water (8 mL) were mixed in a Schlenk-type reaction vessel (30 mL) connected to a gas burette. After the system was purged three times with Ar, 2 mL of a 2 mmol aqueous solution of AB was added into the vessel to react at 30 °C. The reaction progress was evaluated by the amount of evolved H_2. TOF values were calculated as (H_2 mol)/((total Ru mol) min).

DFT calculations

All calculations were performed using the DMol3 program in the Materials Studio 17.2 software package.[57,58] The generalized gradient approximation (GGA) exchange-correlation functional proposed by Perdew, Burke, and Ernzerhof (PBE) was used. This function was combined with the double-numerical basis set plus polarization functions (DNP) in conjunction with a cutoff value of 4.0 Å. We adopted the medium level in the DMol^3 program for the integration grid.

The simulations of hydrogen spillover on reducible metal oxides were conducted using 3 × 3 rutile TiO_2 (110) supercell with a cell dimension of 5.918 × 12.994 × 20.785 Å, 3 × 3 CeO_2

(001) supercell with a cell dimension of 11.479 × 11.479 × 19.058 Å and 3 × 3 WO_3 (001) supercell with a cell dimension of 10.662 × 10.662 × 21.070 Å, respectively. Herein, rutile TiO_2 was used as the TiO_2 model because the hydrogen spillover mechanism over anatase TiO_2 was thoroughly investigated in other reports.[6,52,59,60] The number of oxide layers was 4, 4, and 3 for TiO_2 (110), CeO_2 (001) and WO_3 (001) planes, respectively. The slab was separated by a vacuum space with a height of 15 Å and tetrahedral Ru_5 clusters were loaded on the surface of each oxide. The reactant atoms, Ru cluster and top oxide layer were relaxed during geometry optimizations and the other layers were fixed at the corresponding bulk positions. Transition states (TSs) were determined by the nudged elastic band method and the activation energy was defined by the energy difference between the TS and the reactant.

Data availability

All data generated and analyzed during this study are included in this article and its ESI,† or are available from the corresponding authors upon reasonable request.

Author contributions

K. S. performed the catalyst preparation, calculation, and characterization. K. M. supervised the project, performed a part of calculation, and wrote the manuscript. S. M. and N. H. helped the catalyst preparation and characterization. Y. H. provided advice on analysing calculations. H. K. helped calculations. H. Y. helped supervise the project. The manuscript was written through the discussion with all authors. All authors have given approval to the final version of manuscript.

Conflicts of interest

There are no conflicts to declare.

Acknowledgements

Notes and references

1 R. Prins, *Chem. Rev.*, 2012, **112**, 2714–2738.
2 M. Choi, S. Yook and H. Kim, *ChemCatChem*, 2015, **7**, 1048–1057.
3 K. Murakami and Y. Sekine, *Phys. Chem. Chem. Phys.*, 2020, **22**, 22852–22863.
4 M. Xiong, Z. Gao and Y. Qin, *ACS Catal.*, 2021, **11**, 3159–3172.
5 P. A. Sermon and G. C. Bond, *Catal. Rev.*, 1974, **8**, 211–239.
6 W. Karim, C. Spreafico, A. Kleibert, J. Gobrecht, J. VandeVondele, Y. Ekinci and J. A. van Bokhoven, *Nature*, 2017, **541**, 68–71.
7 K. Liu, P. Yan, H. Jiang, Z. Xia, Z. Xu, S. Bai and Z. C. Zhang, *J. Catal.*, 2019, **369**, 396–404.
8 T. M. David, K. I. Gnanasekar, P. Wilson, P. Sagayaraj and T. Mathews, *ACS Omega*, 2020, **5**, 11352–11360.
9 C. Mao, J. Wang, Y. Zou, G. Qi, J. Y. Yang Loh, T. Zhang, M. Xia, J. Xu, F. Deng, M. Ghoussoub, N. P. Kherani, L. Wang, H. Shang, M. Li, J. Li, X. Liu, Z. Ai, G. A. Ozin, J. Zhao and L. Zhang, *J. Am. Chem. Soc.*, 2020, **142**, 17403–17412.
10 K. Mori, N. Hashimoto, N. Kamiuchi, H. Yoshida, H. Kobayashi and H. Yamashita, *Nat. Commun.*, 2021, **12**, 3884.
11 M. Pudukudy, Z. Yaakob, Q. Jia and M. Sobri Takriff, *New J. Chem.*, 2018, **42**, 14843–14856.
12 Y. Nakagawa, S. Tazawa, T. Wang, M. Tamura, N. Hiyoshi, K. Okumura and K. Tomishige, *ACS Catal.*, 2017, **8**, 584–595.
13 Z. Peng, Z. Li, Y.-Q. Liu, S. Yan, J. Tong, D. Wang, Y. Ye and S. Li, *Chem. Commun.*, 2017, **53**, 5958–5961.
14 H. Cheng, M. Wen, X. Ma, Y. Kuwahara, K. Mori, Y. Dai, B. Huang and H. Yamashita, *J. Am. Chem. Soc.*, 2016, **138**, 9316–9324.
15 Y. F. Li, N. Soheilnia, M. Greiner, U. Ulmer, T. Wood, A. A. Jelle, Y. Dong, A. P. Yin Wong, J. Jia and G. A. Ozin, *ACS Appl. Mater. Interfaces*, 2019, **11**, 5610–5615.
16 J. Park, S. Lee, H.-E. Kim, A. Cho, S. Kim, Y. Ye, J. W. Han, H. Lee, J. H. Jang and J. Lee, *Angew. Chem., Int. Ed.*, 2019, **58**, 16038–16042.
17 R. Prins, V. K. Palfi and M. Reiher, *J. Phys. Chem. C*, 2012, **116**, 14274–14283.
18 S. Khoobiar, *J. Phys. Chem.*, 1964, **68**, 411–412.
19 N. M. Briggs, L. Barrett, E. C. Wegener, L. V. Herrera, L. A. Gomez, J. T. Miller and S. P. Crossley, *Nat. Commun.*, 2018, **9**, 3827.
20 J. Im, H. Shin, H. Jang, H. Kim and M. Choi, *Nat. Commun.*, 2014, **5**, 3370.
21 J. Zhang, Z. Gao, S. Wang, G. Wang, X. Gao, B. Zhang, S. Xing, S. Zhao and Y. Qin, *Nat. Commun.*, 2019, **10**, 4166.
22 M. Xiong, Z. Gao, P. Zhao, G. Wang, W. Yan, S. Xing, P. Wang, J. Ma, Z. Jiang, X. Liu, J. Ma, J. Xu and Y. Qin, *Nat. Commun.*, 2020, **11**, 4773.
23 S. K. Beaumont, S. Alayoglu, C. Specht, N. Kruse and G. A. Somorjai, *Nano Lett.*, 2014, **14**, 4792–4796.
24 M. Takabatake, A. Hashimoto, W.-J. Chun, M. Nambo, Y. Manaka and K. Motokura, *JACS Au*, 2021, **1**, 124–129.
25 R. C. Maher, P. R. Shearing, E. Brightman, D. J. L. Brett, N. P. Brandon and L. F. Cohen, *Adv. Sci.*, 2016, **3**, 1500146.
26 S. K. Konda and A. Chen, *Mater. Today*, 2016, **19**, 100–108.
27 M. P. Suh, H. J. Park, T. K. Prasad and D.-W. Lim, *Chem. Rev.*, 2012, **112**, 782–835.
28 G. Dutta, U. V. Waghmare, T. Baidya and M. S. Hegde, *Chem. Mater.*, 2007, **19**, 6430–6436.
29 S. S. E. Collins, M. Cittadini, C. Pecharromán, A. Martucci and P. Mulvaney, *ACS Nano*, 2015, **9**, 7846–7856.

30 M. Horprathum, T. Srichaiyaperk, B. Samransuksamer, A. Wisitsoraat, P. Eiamchai, S. Limwichean, C. Chananonnawathorn, K. Aiempanakit, N. Nuntawong, V. Patthanasettakul, C. Oros, S. Porntheeraphat, P. Songsiriritthigul, H. Nakajima, A. Tuantranont and P. Chindaudom, *ACS Appl. Mater. Interfaces*, 2014, **6**, 22051–22060.

31 L. Jiang, K. Liu, S.-F. Hung, L. Zhou, R. Qin, Q. Zhang, P. Liu, L. Gu, H. M. Chen, G. Fu and N. Zheng, *Nat. Nanotechnol.*, 2020, **15**, 848–853.

32 M. Torimoto, K. Murakami and Y. Sekine, *Bull. Chem. Soc. Jpn.*, 2019, **92**, 1785–1792.

33 M. Torimoto, S. Ogo, D. Harjowinoto, T. Higo, J. G. Seo, S. Furukawa and Y. Sekine, *Chem. Commun.*, 2019, **55**, 6693–6695.

34 G. Kyriakou, M. B. Boucher, A. D. Jewell, E. A. Lewis, T. J. Lawton, A. E. Baber, H. L. Tierney, M. Flytzani-Stephanopoulos and E. C. H. Sykes, *Science*, 2012, **335**, 1209–1212.

35 S. Kato, M. Ammann, T. Huthwelker, C. Paun, M. Lampimäki, M.-T. Lee, M. Rothensteiner and J. A. van Bokhoven, *Phys. Chem. Chem. Phys.*, 2015, **17**, 5078–5083.

36 S. Alayoglu, K. An, G. Melaet, S. Chen, F. Bernardi, L. W. Wang, A. E. Lindeman, N. Musselwhite, J. Guo, Z. Liu, M. A. Marcus and G. A. Somorjai, *J. Phys. Chem. C*, 2013, **117**, 26608–26616.

37 H. Yin, L.-Q. Zheng, W. Fang, Y.-H. Lai, N. Porenta, G. Goubert, H. Zhang, H.-S. Su, B. Ren, J. O. Richardson, J.-F. Li and R. Zenobi, *Nat. Catal.*, 2020, **3**, 834–842.

38 H. Yoon, Y. Kim, E. J. Crumlin, D. Lee, K. Ihm and J. Son, *J. Phys. Chem. Lett.*, 2019, **10**, 7285–7292.

39 K. Mori, K. Miyawaki and H. Yamashita, *ACS Catal.*, 2016, **6**, 3128–3135.

40 S. Masuda, K. Mori, T. Sano, K. Miyawaki, W.-H. Chiang and H. Yamashita, *ChemCatChem*, 2018, **10**, 3526–3531.

41 S. Masuda, K. Shun, K. Mori, Y. Kuwahara and H. Yamashita, *Chem. Sci.*, 2020, **11**, 4194–4203.

42 G. Chen, S. Desinan, R. Rosei, F. Rosei and D. Ma, *Chem.–Eur. J.*, 2012, **18**, 7925–7930.

43 Z. Helali, A. Jedidi, O. A. Syzgantseva, M. Calatayud and C. Minot, *Theor. Chem. Acc.*, 2017, **136**, 100.

44 V. Vorotnikov, T. R. Eaton, A. E. Settle, K. Orton, E. C. Wegener, C. Yang, J. T. Miller, G. T. Beckham and D. R. Vardon, *ACS Catal.*, 2019, **9**, 11350–11359.

45 S. Ghoshal, A. Pramanik and P. Sarkar, *Phys. Chem. Chem. Phys.*, 2021, **23**, 1527–1538.

46 G.-X. Ge, H.-X. Yan, Q. Jing and Y.-H. Luo, *J. Cluster Sci.*, 2011, **22**, 473.

47 R. C. Nelson, B. Baek, P. Ruiz, B. Goundie, A. Brooks, M. C. Wheeler, B. G. Frederick, L. C. Grabow and R. N. Austin, *ACS Catal.*, 2015, **5**, 6509–6523.

48 G.-J. Xia, M.-S. Lee, V.-A. Glezakou, R. Rousseau and Y.-G. Wang, *ACS Catal.*, 2022, **12**, 4455–4464.

49 A. R. Puigdollers and G. Pacchioni, *ChemCatChem*, 2017, **9**, 1119–1127.

50 Y. Hinuma, T. Toyao, N. Hamamoto, M. Takao, K.-i. Shimizu and T. Kamachi, *J. Phys. Chem. C*, 2020, **124**, 27621–27630.

51 T. Whittaker, K. B. S. Kumar, C. Peterson, M. N. Pollock, L. C. Grabow and B. D. Chandler, *J. Am. Chem. Soc.*, 2018, **140**, 16469–16487.

52 S. Wang, Z. J. Zhao, X. Chang, J. Zhao, H. Tian, C. Yang, M. Li, Q. Fu, R. Mu and J. Gong, *Angew. Chem., Int. Ed.*, 2019, **58**, 7668–7672.

53 F. Peng, W. Yu, Y. Lu, Y. Sun, X. Fu, J. m. Hao, X. Chen, R. Cong and N. Dai, *ACS Appl. Mater. Interfaces*, 2020, **12**, 41230–41238.

54 H. E. Kissinger, *Anal. Chem.*, 1957, **29**, 1702–1706.

55 Y. Tang, Y. Kobayashi, K. Shitara, A. Konishi, A. Kuwabara, T. Nakashima, C. Tassel, T. Yamamoto and H. Kageyama, *Chem. Mater.*, 2017, **29**, 8187–8194.

56 B. Ravel and M. Newville, *J. Synchrotron Radiat.*, 2005, **12**, 537–541.

57 B. Delley, *J. Chem. Phys.*, 1990, **92**, 508–517.

58 B. Delley, *J. Chem. Phys.*, 2000, **113**, 7756–7764.

59 A. Sihag, Z.-L. Xie, H. V. Thang, C.-L. Kuo, F.-G. Tseng, M. S. Dyer and H.-Y. T. Chen, *J. Phys. Chem. C*, 2019, **123**, 25618–25627.

60 H.-Y. T. Chen, S. Tosoni and G. Pacchioni, *ACS Catal.*, 2015, **5**, 5486–5495.